Nano Research

Open Access

Research Article

Multiscale-coupled triple-confinement engineering: Fabrication and applications of high-efficiency long-lifetime room-temperature phosphorescent carbon dots

Kaixiang Cui[1,2], Keyu Xie[1], Haonan Peng[1] ✉, Liping Ding[1] ✉, and Yu Fang[1]

[1] *Key Laboratory of Applied Surface and Colloid Chemistry of Ministry of Education, Shaanxi Provincial Key Laboratory of New Concept Sensors and Molecular Materials, School of Chemistry and Chemical Engineering, Shaanxi Normal University, Xi'an 710119, China*
[2] *School of Petroleum and Environmental Engineering, Yan'an University, Yan'an 716000, China*

Cite this article: *Nano Research*, **2026**, *19*, 94908629. https://doi.org/10.26599/NR.2026.94908629

ABSTRACT: The practical application of carbon dots (CDs) in room-temperature phosphorescence (RTP) is fundamentally constrained by the inherent trade-off between phosphorescence lifetime and quantum yield within conventional single-confinement systems. Herein, we report a multiscale-coupled triple-confinement paradigm that integrates molecular-level covalent locking (C=N bonds), nanoscale silica encapsulation, and matrix-level boron oxide rigidification. This synergistic design decouples the competing requirements of enhanced intersystem crossing (ISC) and suppressed nonradiative decay, enabling nonlinear performance amplification with a synergy index S = 2.4 (> 1). The optimized CD@SiO_2@B_2O_3 composite exhibits an exceptional phosphorescence lifetime of 1119.8 ms and a quantum yield of 25.98%, corresponding to 3.8-fold and 1.7-fold enhancements relative to single-confinement CD@B_2O_3 (291.4 ms and 15.35%), respectively. Systematic mechanistic investigations confirm that C=N bonds reduce the singlet-triplet energy gap (ΔE_{ST}) by 0.14 eV to facilitate ISC, whereas the hybrid matrix suppresses nonradiative decay rate by 77.2% (from 2.90 to 0.66 s^{-1}). This strategy is readily extendable to other systems and exhibits excellent universality. Furthermore, leveraging phosphorescence resonance energy transfer (PRET) with trace amounts (1 wt.%) of fluorescent dyes enables multicolor RTP tunability while preserving hundreds-millisecond lifetimes, overcoming the emission color restriction of traditional RTP CDs. These merits enable applications including time-gated information encryption with second-level temporal resolution, high-contrast fingerprint visualization on multicolor substrates, and warm-white light-emitting diodes (LEDs) free of commercial phosphors. This work establishes a universal design principle for multiscale-coupled confinement, providing a robust platform for next-generation high-performance RTP materials.

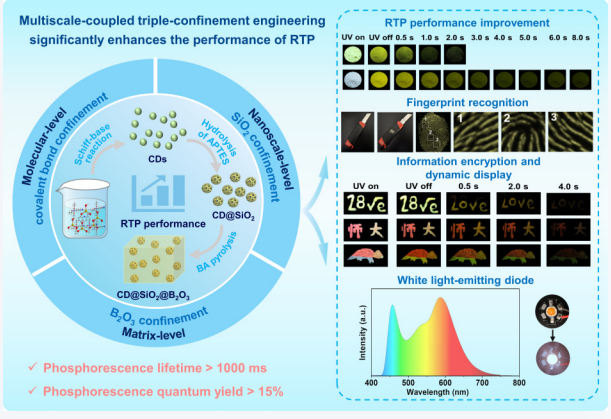

KEYWORDS: room-temperature phosphorescence, carbon dots, structural confinement, synergistic enhancement, phosphorescence resonance energy transfer

1 Introduction

Room-temperature phosphorescence (RTP) materials have garnered significant attention due to their wide-ranging applications in anti-counterfeiting, biological imaging, information encryption, and optoelectronic devices [1–6]. Unlike traditional fluorescence, RTP materials exhibit exceptionally prolonged emission lifetimes, typically ranging from milliseconds to seconds after excitation ceases, arising from spin-forbidden transitions from the excited triplet state back to the ground state [7–9]. This distinctive property has spurred extensive research into the development of efficient RTP systems [10–12]. Nonetheless, conventional RTP materials based on rare-earth elements or transition-metal complexes suffer from notable drawbacks such as high toxicity, environmental hazards, and complex synthetic

Received: January 11, 2026; **Revised:** March 5, 2026
Accepted: March 10, 2026

✉Address correspondence to Haonan Peng, phn@snnu.edu.cn; Liping Ding, dinglp33@snnu.edu.cn

processes, severely constraining their practical utility [13, 14]. Thus, developing efficient and green RTP materials has emerged as a critical research focus.

In recent years, carbon dots (CDs), a new class of zero-dimensional carbon-based nanomaterials, have emerged as promising candidates for RTP applications due to their remarkable biocompatibility, low toxicity, and tunable optical properties [15–17]. CDs possess unique photoluminescence characteristics and can be precisely engineered through rational structural and surface chemistry design [18, 19]. Their inherent advantages, including simple synthesis, excellent photostability, and versatile surface functionalization capabilities, make CDs highly attractive as metal-free RTP emitters [20–22]. However, achieving efficient and long-lifetime RTP of CDs remains fundamentally challenging due to: (1) weak spin-orbit coupling, which hinders effective intersystem crossing (ISC) from singlet to triplet states; (2) rapid non-radiative decay pathways driven by molecular vibrations and oxygen quenching; and (3) aggregation-induced quenching effects in solid-state systems [23–25].

To address these challenges, various strategies have been employed to enhance the RTP performance of CDs. It is worth noting that the RTP performance of carbon dots is closely related to their luminescence mechanism. Effectively enhancing the ISC process and inhibiting the non-radiative transition process of the lowest excited state (T1) is the key to obtaining high-performance RTP materials [26, 27]. Embedding the CD into a rigid matrix (such as borate, polyvinyl alcohol, or silica) or through chemical bond linking has been proven to effectively restrict molecular movement and inhibit non-radiative transitions [28–30]. For example, Gong et al. constructed a stable rigid network through synergistic boric acid (BA) and silane interactions, resulting in dual-mode emitting CDs with a lifetime of 450 ms [31]. Shi et al. synthesized blue phosphorescent CDs with a lifetime of 315 ms, employing covalent cross-linked structures involving Si–O–Si, Si–O–C, and Si–C bonds to constrain molecular vibrations [32]. Yang et al. demonstrated an RTP lifetime up to 1.01 s by embedding CDs into a dicyandiamide matrix via hydrogen bonding and spatial confinement effects [33]. Despite these advancements, existing RTP CDs still face critical limitations, including phosphorescence lifetimes generally shorter than 1 s, quantum yields typically below 10%, and emission predominantly confined to blue or green regions. These constraints significantly impede their broader practical applications. A critical unresolved challenge is that these isolated confinement effects cannot simultaneously suppress both ISC bottleneck and nonradiative decay, creating a performance ceiling [34, 35].

Recognizing this intrinsic limitation, we hypothesize that multiscale-coupled confinement, integrating molecular, nanoscale, and matrix-level restrictions, could decouple these competing factors and trigger synergistic amplification. Herein, we report a triple-confinement engineering approach: (1) Covalent locking via Schiff-base C=N bonds enhances spin-orbit coupling (SOC) and reduces the singlet-triplet energy gap (ΔE_{ST}). (2) SiO_2 encapsulation via 3-aminopropyltriethoxysilane (APTES) hydrolysis provides nanoscale steric hindrance. (3) B_2O_3 matrix via boric acid pyrolysis offers macroscopic rigidity. This hierarchical design yields exceptional nonlinear enhancement. Furthermore, leveraging phosphorescence resonance energy transfer (PRET) with trace amounts (1 wt.%) of fluorescent dyes enables color tunability while preserving hundreds-millisecond level lifetimes, overcoming the emission color limitation of conventional RTP CDs and significantly expanding functional applications. This work establishes a universal design principle for high-performance CDs RTP materials.

2 Experimental

2.1 Materials

2-quinolinecarboxaldehyde (2-QCA, ≥ 98.0%), BA (≥ 99.0%), 2,2′-dithiodibenzoic acid (DTHBA, ≥ 96.0%), and bis(trimethoxysilylpropyl)amine (BTMSPA, ≥ 90.0%) were purchased from Aladdin (Shanghai, China). APTES (≥ 98.0%) and rhodamine 6G (RhG, ≥ 95.0%) were obtained from J&K Scientific. Anhydrous ethanol (≥ 99.7%) was purchased from Sinopharm (Shanghai, China). Rhodamine B (RhB, ≥ 95.0%) was purchased from Sigma-Aldrich. All the reagents were commercially available and could be used directly without further purification. Deionized water (18.2 MΩ·cm, 25 °C) purified by a Milli-Q system was used to prepare all aqueous solutions.

2.2 Characterization methods

The morphology and crystalline structure of the synthesized quantum dots were examined using a transmission electron microscopy (TEM, Tecnai G2 F20, FEI). The particle size distribution was analyzed using Nano Measure 1.2 software. Fourier-transform infrared (FT-IR) spectra were recorded on a Vertex 70V FT-IR spectrometer (Bruker, Germany). Powder X-ray diffraction (XRD) patterns were acquired using a Bruker D8 Advance diffractometer. X-ray photoelectron spectroscopy (XPS, Kratos Analytical Co., Ltd.) was employed to analyze the surface chemical composition and valence states of elements within the QDs. Fluorescence and phosphorescence spectra were measured using an F7100 fluorescence spectrophotometer (Hitachi, Japan). Ultraviolet–visible (UV–vis) absorption spectra were recorded using a Lambda 1050 UV–vis–near infrared (NIR) spectrometer (PerkinElmer, USA). Fluorescence and phosphorescence lifetimes were determined by an FLS 980 spectrometer (Edinburgh Instruments, UK). The phosphorescence quantum yields and variable-temperature phosphorescence spectra were measured using a Fluorolog-QM steady-state/transient fluorescence and phosphorescence spectrometer (HORIBA, Japan).

2.3 Preparation of CD@B_2O_3-0 and CD@SiO_2@B_2O_3-2

To synthesize CD@B_2O_3-0, 0.1 g of 2-QCA was dissolved in 2.5 mL of anhydrous ethanol in a 50 mL round-bottom flask via ultrasonication for 10 min. Subsequently, 2.0 g of BA and 27.5 mL of deionized water were added to the solution, followed by stirring at 60 °C for 30 min to initiate a pre-reaction. The resulting mixture was then transferred to a 50.0 mL beaker. The beaker was sealed with aluminum foil, perforated with a needle to allow venting, and placed in an explosion-proof oven. The mixture was thermally treated at 200 °C for 2 h. After cooling naturally to room temperature, the solid product was ground into powder to obtain CD@B_2O_3-0.

The synthesis of CD@SiO_2@B_2O_3-2 followed the same procedure, with the only difference being the addition of 750 μL of APTES alongside 0.1 g of 2-QCA in the initial step. The preparation procedures for other samples are described in detail in the Electronic Supplementary Material (ESM).

3 Results and discussion

3.1 Design and characterization

As shown in Scheme 1, 2-QCA was employed as the carbon precursor, and excess of APTES was used for silica precursor with dual functions. On the one hand, the amino group (–NH_2) of APTES undergoes a Schiff-base condensation with the aldehyde group (–CHO) of 2-QCA, forming molecular-level covalent C=N bonds. On the other hand, APTES is hydrolyzed *in situ* to generate a nanoscale silica encapsulation. Additionally, classical BA serves as a solid-state immobilization medium, forming a matrix-level B_2O_3 rigidification upon thermal treatment. This multiscale-coupled triple confinement engineering of covalent bond link, silica encapsulation, and boron oxide fixation may synergistically enhance the phosphorescence lifetime and phosphorescence quantum yield of the resulting composite materials. In order to better verify this speculation, four different samples were prepared, namely those containing only 2-QCA, only APTES, both APTES and 2-QCA, and both with more APTES, which were termed as CD@B_2O_3-0, CD@SiO_2@B_2O_3-1, CD@SiO_2@B_2O_3-2, and CD@SiO_2@B_2O_3-3, respectively. The specific preparation process can be found in Section 2 and the ESM.

To characterize the structure and morphology of the composite materials, TEM, XRD, FT-IR, and XPS measurements were employed. Using CD@SiO_2@B_2O_3-2 as a representative sample, TEM images (Fig. S1(a) in the ESM) reveal that the sample appears as aggregated chunks after grinding. Higher magnification microscopic images (Fig. S1(b) in the ESM) reveal spherical nanoscale silica nanoparticles, with most of the particle sizes ranging from 70.0 to 110.0 nm, dispersed in the B_2O_3 matrix (Fig. S2 in the ESM). Further magnified TEM image (Fig. 1(a)) reveals that carbon dots are distributed inside the silica matrix. High-resolution TEM (HRTEM) image (Fig. 1(b)) shows that the carbon dots have an average particle size of approximately 3 nm and exhibit distinct lattice fringes. The measured lattice spacing of 0.21 nm corresponds to the (100) plane of graphitic carbon, as determined by Nano Measure 1.2 software, indicating the presence of graphite-like structures within the composites (inset of Fig. 1(b)) [36]. A statistical analysis based on 60 individual particles (Fig. 1(c)) further confirms that the carbon dots are uniformly dispersed, with an average diameter of 3.3 nm.

The structural features of CD@B_2O_3-0, CD@SiO_2@B_2O_3-1, CD@SiO_2@B_2O_3-2, and CD@SiO_2@B_2O_3-3 were investigated using XRD, as shown in Fig. 1(d). All samples exhibit weak diffraction peaks, likely due to their low crystallinity. Wavelet-transformed data reveal three main characteristic peaks at 12.5°, 21.5°, and 42.4°. Notably, the peak at 12.5° is observed only in CD@SiO_2@B_2O_3-1, CD@SiO_2@B_2O_3-2, and CD@SiO_2@B_2O_3-3. This peak is attributed to the (020) facet of SiO_2, confirming its successful incorporation in the three samples [31, 37]. In contrast, this signal is absent in CD@B_2O_3-0. The broad peak at 21.5° corresponds to the instrumental background, consistent with previous reports [38]. The prominent peak at 44.9°, detected in all samples, is assigned to the (111) facet of B_2O_3, indicating that boric acid was successfully converted into a rigid B_2O_3 matrix [23, 37]. Notably, the B_2O_3(111) peak at 44.9° shows gradual broadening with increasing APTES content, indicating that SiO_2 incorporation disrupts B_2O_3 crystallinity, forming a more amorphous and rigid hybrid matrix. This amorphous character is crucial for suppressing energy transfer losses.

The FT-IR spectra (Fig. 1(e)) further confirmed the presence of various functional groups and chemical bonds. A broad absorption band near 3460 cm^{-1} in CD@SiO_2@B_2O_3-1, CD@SiO_2@B_2O_3-2, and CD@SiO_2@B_2O_3-3 corresponds to Si–OH stretching, while characteristic peaks at 1055 and 780 cm^{-1} are associated with C–Si and Si–O bonds, respectively [39, 40]. These peaks are absent in CD@B_2O_3-0, confirming that APTES induced SiO_2 formation. The absorption band near 1630 cm^{-1}, corresponding to the C=N stretching vibration, appears prominently in CD@SiO_2@B_2O_3-2 and CD@SiO_2@B_2O_3-3. This indicates that Schiff-base condensation

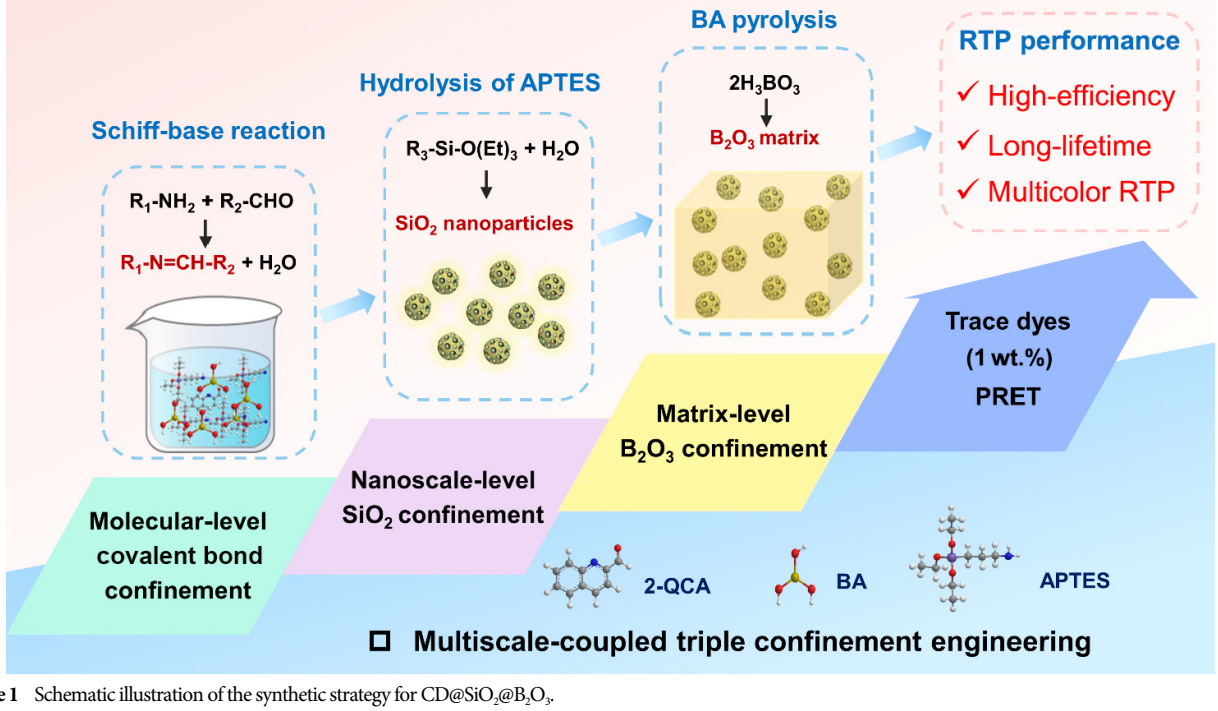

Scheme 1 Schematic illustration of the synthetic strategy for CD@SiO_2@B_2O_3.

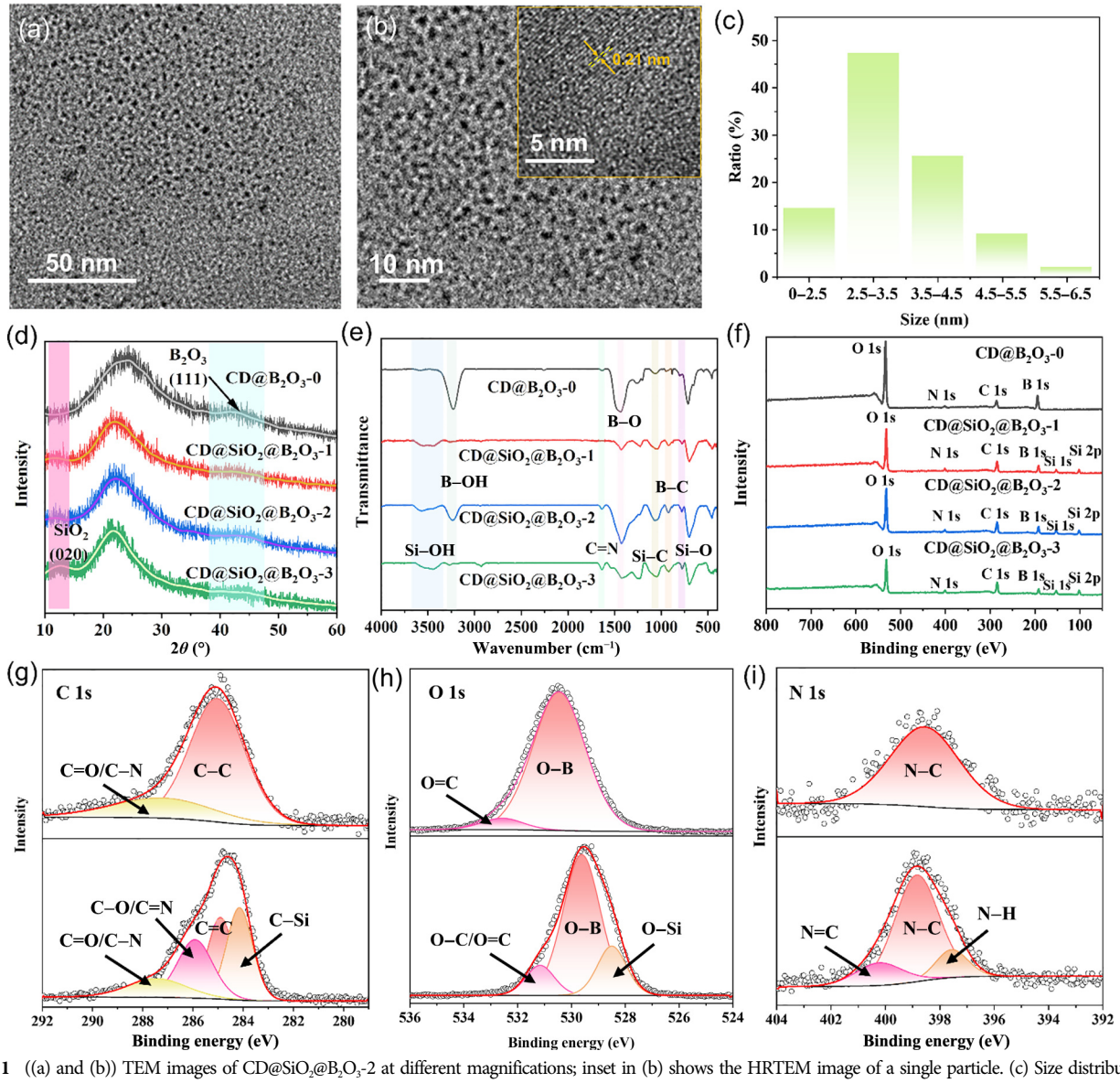

Figure 1 ((a) and (b)) TEM images of $CD@SiO_2@B_2O_3$-2 at different magnifications; inset in (b) shows the HRTEM image of a single particle. (c) Size distribution of CDs derived from statistical analysis of TEM images. (d) XRD patterns, (e) FT-IR spectra, and (f) XPS survey spectra of $CD@SiO_2@B_2O_3$ composite samples. ((g)–(i)) High-resolution XPS spectra of (g) C 1s, (h) O 1s, and (i) N 1s for $CD@B_2O_3$-0 (above) and $CD@SiO_2@B_2O_3$-2 (below).

between APTES and 2-QCA leads to formation of C=N covalent bonds, thereby increasing the rigidity of the matrix. Additional absorption bands at 3240, 1440, and 920 cm^{-1} correspond to B–OH, B–O, and B–C bonds, respectively, which are indicative of B_2O_3 formation [41, 42]. Overall, the FT-IR results confirm the coexistence of C=N bonds and strong rigid matrices composed of SiO_2 and B_2O_3.

XPS measurements were employed to analyze the elemental compositions and bonding environments. The survey spectra (Fig. 1(f)) for $CD@SiO_2@B_2O_3$-1, $CD@SiO_2@B_2O_3$-2, and $CD@SiO_2@B_2O_3$-3 display five major peaks at 531.8, 400.5, 284.8, 191.8, and 101.8 eV, corresponding to O, N, C, B, and Si elements, respectively. $CD@B_2O_3$-0 lacks the Si signal at 101.8 eV, confirming the absence of SiO_2, consistent with FT-IR and XRD findings. The high-resolution C 1s spectra (Fig. 1(g)) show two peaks in $CD@B_2O_3$-0 at 287.3 and 284.8 eV, corresponding to C=O/C–N and C–C bonds, respectively. In $CD@SiO_2@B_2O_3$-2, four distinct peaks were observed at 287.3, 285.9, 284.8, and 284.1 eV, which are attributed to C=O/C–N, C–O/C=N, C–C, and C–Si bonds, respectively, indicating successful incorporation of C=N bond [31, 43]. The C 1s spectrum of $CD@SiO_2@B_2O_3$-1 exhibits three peaks corresponding to C–O, C–C, and C–Si bonds, while $CD@SiO_2@B_2O_3$-3 displays a similar profile to $CD@SiO_2@B_2O_3$-2 (Fig. S3(a) in the ESM). High-resolution O 1s spectra (Fig. 1(h)) reveal an additional peak at 528.5 eV in $CD@SiO_2@B_2O_3$-2, corresponding to O–Si bond, which is also present in $CD@SiO_2@B_2O_3$-1 and $CD@SiO_2@B_2O_3$-3 (Fig. S3(b) in the ESM), supporting the formation of SiO_2. By comparison, the N 1s spectra (Fig. 1(i) and Fig. S3(c) in the ESM) show additional peaks at 400.8 and 397.5 eV in $CD@SiO_2@B_2O_3$-2 and $CD@SiO_2@B_2O_3$-3, corresponding to N=C and N–H bonds, respectively [44]. The absence of the N=C peak at 400.8 eV in $CD@B_2O_3$-0 and $CD@SiO_2@B_2O_3$-1 (Fig. 1(i) and Fig. S3(c) in the ESM) further confirms that the Schiff-base reaction between 2-QCA and APTES introduces molecular-level C=N bonds in the composites [23].

As illustrated in Fig. S4(a) in the ESM, the high-resolution Si 2p

spectra of CD@SiO_2@B_2O_3-1, CD@SiO_2@B_2O_3-2, and CD@SiO_2@B_2O_3-3 exhibit three peaks at 100.5, 99.3, and 98.0 eV, corresponding to SiO_2(gel), SiO_2, and Si–C bonds, respectively [44, 45]. The presence of three distinct silicon chemical environments in the Si 2p spectrum verifies the existence of gradient rigidity from the surface to the core. These results confirm that APTES facilitates the formation of rigid nanoscale SiO_2. The B 1s spectra are displayed in Fig. S4(b) in the ESM. In contrast to CD@B_2O_3-0, an additional B-CO_2 signal at 189.2 eV is observed in CD@SiO_2@B_2O_3-1, CD@SiO_2@B_2O_3-2, and CD@SiO_2@B_2O_3-3. This feature can be ascribed to the co-introduction of APTES and BA, which promotes the crystallization of BA at elevated temperatures and the partial formation of C–B bonds with CDs [43, 46]. Such design strategy is favorable for the formation of the matrix-level B_2O_3.

In summary, TEM, XRD, FT-IR, and XPS analyses demonstrate that the introduction of APTES into the CD@B_2O_3-0 system enables the formation of molecular-level C=N covalent bonds through Schiff-base chemistry, the generation of nanoscale SiO_2 via APTES hydrolysis, and the construction of a rigid triple-confinement architecture in conjunction with B_2O_3. This construction is expected to significantly enhance the structural rigidity and microenvironmental stability of carbon dot luminescent centers, laying a solid foundation for improving their RTP performance.

3.2 Photophysical property

The fundamental photophysical properties of the CD@SiO_2@B_2O_3 composites were systematically investigated. As shown in Fig. 2(a), UV–vis absorption spectra reveal that all four samples exhibit strong absorption in the range of 200–300 nm, attributed to π–π* transitions in the carbon core. Notably, CD@B_2O_3-0, CD@SiO_2@B_2O_3-2, and CD@SiO_2@B_2O_3-3 also display a broad absorption band centered at 450 nm, corresponding to n–π* transitions arising from surface groups such as carbonyl (C=O) or imine (C=N) functionalities [47]. In contrast, the absence of absorption peaks at 450 nm for CD@SiO_2@B_2O_3-1 suggests that C=N and C=O bonds do not exist in the system with only APTES.

A pronounced excitation peak near 250 nm was observed for all samples, consistent with their UV–vis absorption spectra. Fluorescence excitation spectra show that CD@SiO_2@B_2O_3-1 exhibits a strong excitation peak at 350 nm, whereas the other three samples present peaks near 320 nm (Fig. 2(b)). The phosphorescence excitation spectra (Fig. S5 in the ESM) display a

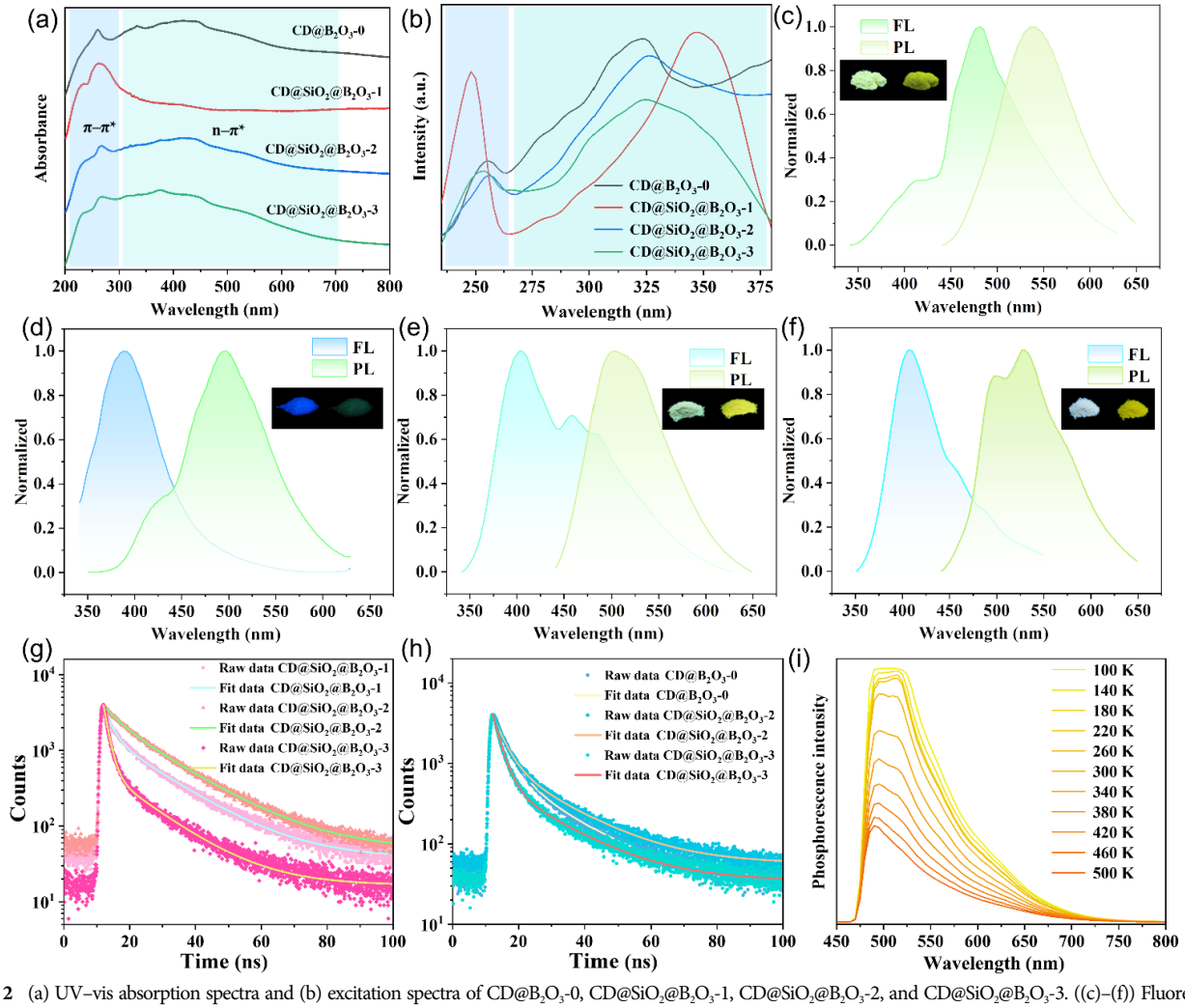

Figure 2 (a) UV–vis absorption spectra and (b) excitation spectra of CD@B_2O_3-0, CD@SiO_2@B_2O_3-1, CD@SiO_2@B_2O_3-2, and CD@SiO_2@B_2O_3-3. ((c)–(f)) Fluorescence and phosphorescence emission spectra of (c) CD@B_2O_3-0, (d) CD@SiO_2@B_2O_3-1, (e) CD@SiO_2@B_2O_3-2, and (f) CD@SiO_2@B_2O_3-3 (insets show corresponding fluorescence and phosphorescence photographs under UV light and afterglow conditions). ((g) and (h)) Fluorescence lifetime decay curves recorded at (g) 400 and (h) 480 nm. (i) Temperature-dependent phosphorescence spectra of CD@SiO_2@B_2O_3-2 from 100 to 500 K.

sharp excitation peak at 320 nm for CD@SiO_2@B_2O_3-1, while the 2-QCA-containing samples exhibit broader excitation bands spanning 300–360 nm. As shown in Fig. S6 in the ESM, the phosphorescence emission peak positions remain unchanged across excitation wavelengths from 300 to 380 nm, although emission intensity varies. The most intense phosphorescence is obtained with 320 nm excitation.

Normalized fluorescence and phosphorescence emission spectra under 320 nm excitation are displayed in Figs. 2(c)–2(f). CD@SiO_2@B_2O_3-1 exhibits emission peaks at 400 (fluorescence) and 500 nm (phosphorescence), while CD@B_2O_3-0 shows the two emission peaks at 480 and 540 nm. CD@SiO_2@B_2O_3-2 emits at 400 nm (fluorescence) and displays a broad phosphorescence band over 500–540 nm. CD@SiO_2@B_2O_3-3 shows fluorescence at 400 nm and dual phosphorescence peaks at 500 and 540 nm. Fluorescence lifetime measurements (Figs. 2(g) and 2(h)) indicate that CD@SiO_2@B_2O_3-1, CD@SiO_2@B_2O_3-2, and CD@SiO_2@B_2O_3-3 have average lifetimes of 12.65, 14.52, and 8.03 ns, respectively, when monitored at 400 nm (Table S1 in the ESM). At 480 nm, the average lifetimes of CD@B_2O_3-0, CD@SiO_2@B_2O_3-2, and CD@SiO_2@B2O3-3 are 9.75, 11.37, and 9.19 ns, respectively (Table S2 in the ESM). The possible reason for the different fluorescence lifetimes is that APTES forms covalent C=N bonds with 2-QCA, thereby restricting non-radiative decay pathways and enhancing radiative transitions. Additionally, the temperature-dependent phosphorescence behavior of CD@SiO_2@B_2O_3-2 was evaluated. As shown in Fig. 2(i), increasing the temperature from 100 to 500 K leads to a gradual decrease in phosphorescence intensity. This trend reflects enhanced non-radiative relaxation at elevated temperatures and confirms the thermal sensitivity of the triplet state dynamics [48].

3.3 RTP performance

Figure 3(a) presents photographs of the phosphorescence emissions from the samples before and after turning off a 365 nm UV lamp under ambient conditions. CD@B_2O_3-0 and CD@SiO_2@B_2O_3-1 exhibited greenish phosphorescence lasting approximately 2.0 (Video S1 in the ESM) and 3.0 s to the naked eye. When both APTES and 2-QCA were introduced, the afterglow duration significantly increases to roughly 5.0 s (Video S2 in the ESM) for CD@SiO_2@B_2O_3-2 and up to 8.0 s (Video S3 in the ESM) for CD@SiO_2@B_2O_3-3, highlighting the synergistic effect of the dual

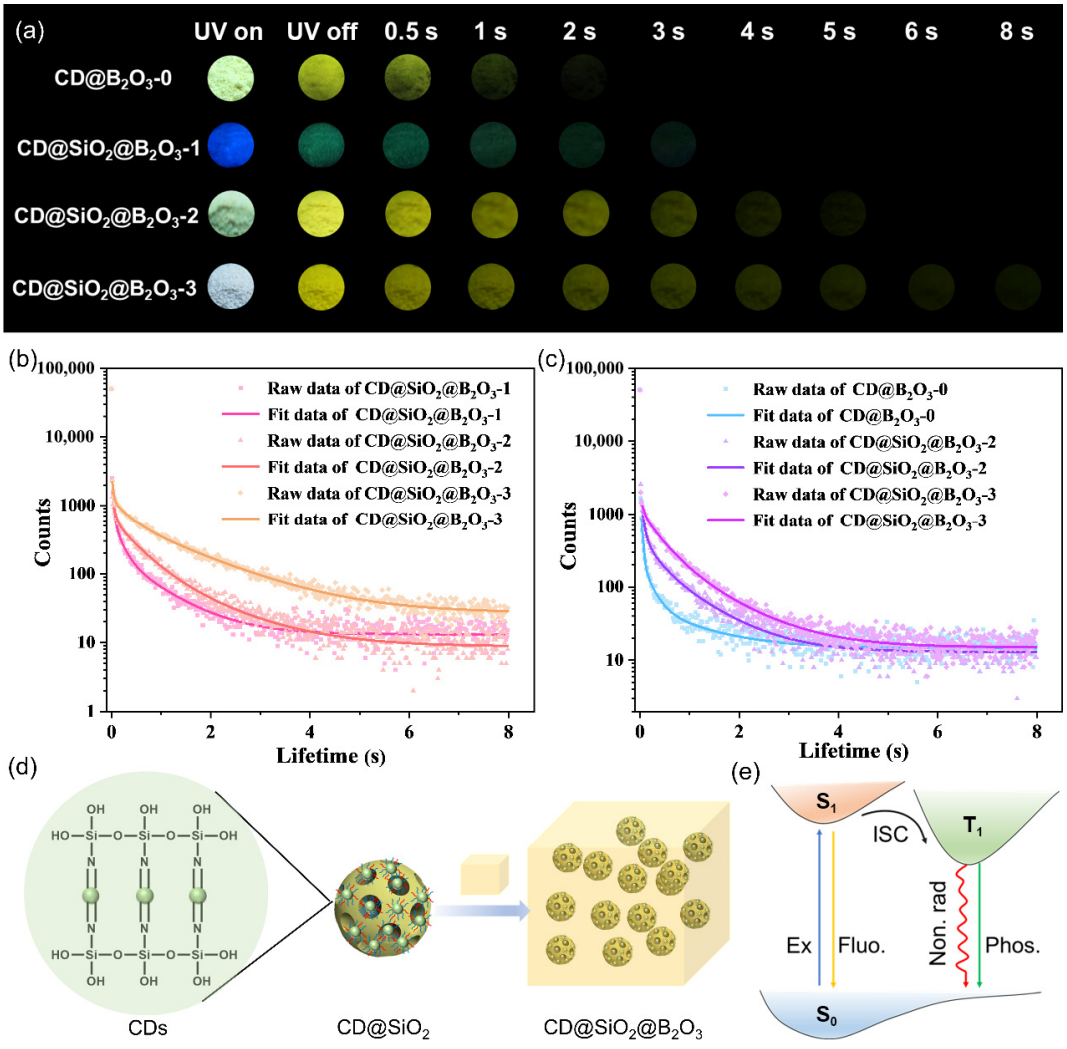

Figure 3 (a) Photographs of CD composite powder excited by 365 nm UV light and after switching off the UV light under ambient conditions. ((b) and (c)) Time-resolved phosphorescence attenuation curves of the CD composite powder monitored at (b) 500 and (c) 540 nm emission band. (d) Schematic diagram of the possible restrictive effects of C=N covalent bonds, SiO_2 entrapment, and B_2O_3 matrix in the CD composites. (e) Energy diagram of phosphorescence emission of CD@SiO_2@B_2O_3 composites (S_0: ground singlet state, S_1: first excited singlet state; and T_1: first excited triplet state).

additives. To quantitatively evaluate the RTP behavior, time-resolved phosphorescence decay profiles were recorded at 500 and 540 nm (Figs. 3(b) and 3(c)). The decay curves were fitted using a triple-exponential function [29], revealing average phosphorescence lifetimes (Tables S3 and S4 in the ESM) of 475.1, 765.2, and 1119.8 ms at 500 nm for CD@SiO_2@B_2O_3-1, CD@SiO_2@B_2O_3-2, and CD@SiO_2@B_2O_3-3, respectively. Corresponding values at 540 nm were 291.4, 597.7, and 686.1 ms for CD@B_2O_3-0, CD@SiO_2@B_2O_3-2, and CD@SiO_2@B_2O_3-3, respectively. Furthermore, a second double-confinement sample, denoted as CD@SiO_2, containing only 2-QCA and APTES (without BA) was also prepared. Its phosphorescence lifetimes at 500 and 540 nm were only 17.1 and 13.6 ms, respectively (Fig. S7 and Table S5 in the ESM). The quantitative phosphorescence lifetime test results further demonstrated the effectiveness of the triple confinement strategy. Additionally, CD@SiO_2@B_2O_3-2 achieved a phosphorescence quantum yield of 25.98%, which is over 10% higher than CD@B_2O_3-0 (15.35%) and CD@SiO_2@B_2O_3-1 (9.61%) (Fig. S8 in the ESM). It is worth noting that the phosphorescence quantum yield shows an ultra-linear increase with the increase of confinement: The phosphorescence quantum yield without adding 2-QCA decreased by 37%, but the further introduction of C=N bonds increased the phosphorescence quantum yield by 170%, which confirms the existence of the synergistic effect. Interestingly, the phosphorescence quantum yield of CD@SiO_2@B_2O_3-3 is 16.52%, indicating that an excessive addition of APTES may reduce the effect of enhancing the quantum yield. Compared with room-temperature phosphorescent carbon dot-based materials prepared by similar methods in recent years, the CD@SiO_2@B_2O_3 fabricated in this work not only exhibits a phosphorescence lifetime of over 1000 ms, but also maintains a phosphorescence quantum yield of over 15% (Table S6 in the ESM). Furthermore, taking CD@SiO_2@B_2O_3-2 as a representative example, the long-term stability of this material was evaluated. The average phosphorescence lifetime at 540 nm decreased by only 5% after 120 days, while the decay profile remains almost unchanged (Fig. S9 and Table S7 in the ESM), demonstrating its excellent long-term stability.

A mechanistic illustration is presented in Fig. 3(d) to elucidate the enhancement of RTP properties via multiscale-coupled triple confinements. The Schiff-base condensation between 2-QCA and APTES forms covalent C=N bonds that promote enhanced conjugation and spin-orbit coupling, facilitating ISC. Simultaneously, the hydrolysis of APTES generates a rigid SiO_2 network that restricts molecular motion, and pyrolytic conversion of BA forms a B_2O_3 matrix that further enhances rigidity. Theoretical calculations confirm a decrease in the singlet-triplet energy gap (ΔE) from 2.16 to 2.02 eV upon C=N bond formation (Fig. S10 in the ESM), supporting the proposed ISC enhancement assumption. The combined spatial and covalent confinements effectively suppress non-radiative decay pathways [49], stabilize triplet excitons, and enhance both lifetime and efficiency of RTP emission (Fig. 3(e)). By simultaneously using the fundamental kinetic equations of excited-state decay (500 nm), the calculation revealed that the nonradiative decay rate k_{nr} decreased by approximately 77.2% (from 2.90 to 0.66 s^{-1}), while the radiative rate k_r remained relatively stable (from 0.43 to 0.39 s^{-1}).

To deconvolute the contributions of different confinement layers and verify the existence of a synergistic effect, we proposed the concept of synergy index (S). This index is defined to quantify the extent to which the performance enhancement of the triple-confinement system exceeds the simple superposition of enhancements from the double-confinement systems. The calculation equation is defined as follows: $S = (\tau_{triple} - \tau_{single})/[(\tau_{double1} + \tau_{double2}) - \tau_{single}]$. Here, τ_{single}, $\tau_{double1}$, $\tau_{double2}$, and τ_{triple} represent the phosphorescence lifetimes of the CD samples prepared from the single-confinement (CD@B_2O_3), double-confinement (two different compositions, CD@SiO_2 and CD@SiO_2@B_2O_3-1), and triple-confinement strategy (CD@SiO_2@B_2O_3-2), respectively. $S > 1$ indicates a positive synergistic effect, where the combined performance is superior to the simple addition of individual contributions. In this work, the calculated $S = 2.4$ (500 nm), which is significantly greater than 1. This result directly confirms that the triple-confinement strategy achieves a true synergistic effect rather than a simple additive effect, which is consistent with our previous analysis.

3.4 Universal applicability of strategy

To validate the universality of this strategy, BTMSPA was employed as an alternative silanization reagent in place of APTES, while keeping all other conditions unchanged and retaining 2-QCA as the carbon source. This substitution was designed to investigate whether the enhanced RTP effect could be preserved when using different silanization reagents. The resulting sample, designated as CD@SiO_2@B_2O_3-4, exhibited a fluorescence emission maximum at 402 nm and a phosphorescence emission maximum at 540 nm (Fig. S11(a) in the ESM). Notably, the phosphorescence lifetime at 540 nm was significantly prolonged to 838.6 ms (Fig. S11(b) and Table S4 in the ESM), representing a 2.9-fold enhancement relative to the singly confined counterpart. These results confirm that the formation of C=N structures and the consequent enhancement of RTP performance can still be achieved even when employing structurally diverse amine-functionalized silanization precursors.

Furthermore, the robustness of this strategy was evaluated by varying the carbon source. With all other parameters kept constant, the aldehyde-containing precursor 2-QCA was replaced by the carboxyl-bearing DTHBA, yielding the samples designated as CD@B_2O_3-5 and CD@SiO_2@B_2O_3-6. Under these conditions, the carboxyl groups of DTHBA underwent condensation with the amino groups of APTES to form amide bonds (CONH) at the molecular level, concurrently with the formation of nanoscale SiO_2 and B_2O_3 matrices. Comparative analysis revealed that CD@SiO_2@B_2O_3-6 exhibited a phosphorescence lifetime of 64.2 ms at 450 nm, corresponding to a 3.7-fold enhancement relative to the 17.2 ms observed for CD@B_2O_3-5 (Fig. S12 and Table S8 in the ESM).

These systematic investigations confirm that the multiscale-coupled triple-confinement strategy possesses excellent universality in enhancing the RTP of carbon dot-based materials. Several general design principles are summarized below: Aromatic precursors functionalized with aldehyde or carboxyl groups are favorable, as they can form stable C=N or CONH covalent bonds with amine-functionalized silanes, thus enabling molecular-level confinement. A variety of amine-containing alkoxysilanes (e.g., APTES and BTMSPA) can be employed, provided that they are capable of reacting with carbon precursors and undergoing hydrolysis to form silica networks.

3.5 Color-tunable RTP carbon dots via PRET

To further expand the functional applications of the developed

carbon dots, trace amounts of commercial fluorescent dyes RhB and RhG were introduced during the synthesis of CD@SiO_2@B_2O_3-2. The resulting materials, CD@SiO_2@B_2O_3-RhB and CD@SiO_2@B_2O_3-RhG, exhibited multicolor RTP emission characteristics. As shown in Fig. 4(a), CD@SiO_2@B_2O_3-RhB displayed orange-red fluorescence under UV light and orange phosphorescence persisting for approximately 5.0 s. Similarly, CD@SiO_2@B_2O_3-RhG showed dark pink fluorescence and yellow afterglow lasting around 6.0 s.

Figure 4(b) illustrates the emission spectra. CD@SiO_2@B_2O_3-RhB featured fluorescence peaks at 400 and 600 nm and phosphorescence peaks at 500 and 592 nm. For CD@SiO_2@B_2O_3-RhG, a similar dual-emission pattern was observed with a minor red shift in peaks (Fig. S13(a) in the ESM). Time-resolved phosphorescence decay curves revealed lifetimes of 634.4 ms at 500 nm and 486.5 ms at 592 nm for CD@SiO_2@B_2O_3-RhB (Fig. 4(c) and Table S9 in the ESM), while CD@SiO_2@B_2O_3-RhG showed corresponding lifetimes of 752.7 and 559.9 ms at 500 and 562 nm, respectively (Fig. S13(b) and Table S10 in the ESM). These results confirm that trace dye doping enables effective tuning of RTP color output.

As illustrated in Fig. 4(d), the enhanced RTP arises from the triply confined CD@SiO_2@B_2O_3-2, which effectively stabilizes triplet excitons and suppresses non-radiative decay through covalent C=N bonding and rigid SiO_2 and B_2O_3 matrices. This long-lived phosphorescent matrix acts as an energy donor, while RhB and RhG dyes serve as acceptors in a triplet-to-singlet Förster-type phosphorescence resonance energy transfer mechanism [50, 51]. The phosphorescence spectra of control samples upon excitation at 320 nm further confirmed this assumption (Fig. S14 in the ESM). SiO_2@B_2O_3-RhB and SiO_2@B_2O_3-RhG without 2-QCA showed almost no phosphorescence emission, while CD@SiO_2@B_2O_3-RhB and CD@SiO_2@B_2O_3-RhG exhibited obvious phosphorescence emission in contrast. Despite using a non-optimal excitation wavelength (320 nm), efficient energy transfer occurs, resulting in tunable multicolor RTP emission and expanding the application scope of the material in optical encryption and anti-counterfeiting technologies.

3.6 Applications in information encryption, fingerprint recognition, and anti-counterfeiting

The exceptional optical properties and tunable multicolor emission of CD@SiO_2@B_2O_3 materials and their derivatives were further explored for practical applications. Their ability to perform time-resolved information encryption was evaluated using CD@SiO_2@B_2O_3-2 and CD@B_2O_3-0, which exhibit different afterglow durations. Utilizing the phosphorescence lifetime (0.83 s) difference, we design a dual-channel encryption with 2.0 s of gate time. As shown in Fig. 5(a), the text "71" and "Love" were written using CD@SiO_2@B_2O_3-2, while "91" and "28 $\sqrt{e}$" were written with CD@B_2O_3-0. Under a 365 nm UV lamp, all patterns are visible. However, within 2.0 s after switching off the lamp, only the longer-lived "71" and "Love" remained visible (Videos S4 and S5 in the ESM), demonstrating an effective time-gated encryption display.

Phosphorescent fingerprint imaging was also demonstrated as a promising alternative to traditional fluorescence-based identification. On a dark substrate, fingerprints were visualized using CD@SiO_2@B_2O_3-2, revealing clear structural details such as

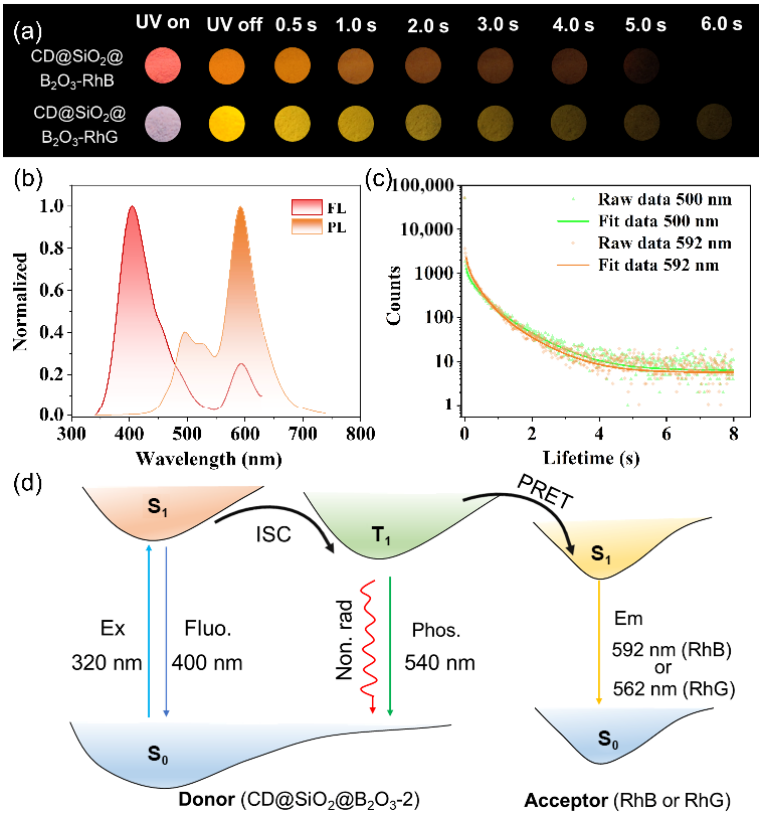

Figure 4 (a) Photographs of CD@SiO_2@B_2O_3-RhB (RhG) powder excited by 365 nm UV light and after switching off the UV light under ambient. (b) Fluorescence and phosphorescence spectra of CD@SiO_2@B_2O_3-RhB. (c) Time-resolved phosphorescence attenuation curves of CD@SiO_2@B_2O_3-RhB. (d) PRET mechanism in CD@SiO_2@B_2O_3/RhB (RhG) composites.

Figure 5 (a) Time-resolved information encryption based on CD@B_2O_3-0 and CD@SiO_2@B_2O_3-0 ("71" and "Love"). (b) Fingerprint recognition on different substrates based on CD@SiO_2@B_2O_3-2 (on knife) and CD@SiO_2@B_2O_3-RhB (on notebook). (c) Multicolor anti-counterfeiting for Chinese characters and animal patterns.

ridge bifurcations, pores, and line breaks (Fig. 5(b)). On a blue notebook background, CD@SiO_2@B_2O_3-RhB was used instead, with its orange phosphorescence offering high contrast, enabling identification of features like scars and ridge breaks. This highlights the potential of these materials for non-invasive and high-contrast forensic applications.

Finally, a multicolor anti-counterfeiting application was illustrated in Fig. 5(c) and Video S6 in the ESM. Characters "师" and "大" were written with CD@SiO_2@B_2O_3-RhB and CD@SiO_2@B_2O_3-RhG, respectively. Under UV light and after switching it off, the characters exhibited distinguishable color transitions from orange-red to orange-yellow for "师" and from dark pink to yellow for "大" with visible afterglow lasting over 4.0 s. A multicolored turtle image was also fabricated using different CD@SiO_2@B_2O_3 samples for each body part. Upon UV excitation and decay, a dynamic display of color transitions was observed, underscoring the excellent potential of these materials in multicolor display technologies and high-security anti-counterfeiting applications.

3.7 Application in warm white light-emitting diodes (WLEDs)

Given the excellent luminescent properties of the synthesized CD@SiO_2@B_2O_3 materials, their application in WLEDs was further explored [52]. Initially, CD@SiO_2@B_2O_3-2 was mixed with a UV-curable adhesive and coated onto a 365 nm LED chip to fabricate a monochromatic LED. The resulting electroluminescence (EL) spectrum, shown in Fig. 6(a), exhibited a broad emission band ranging from 460 to 600 nm, corresponding to green-to-orange-yellow light. The chromaticity coordinates of this device are presented in Fig. S15(a) in the ESM. Subsequently, CD@SiO_2@B_2O_3-RhB was similarly processed with the UV-curable adhesive and applied to a 365 nm LED chip. As depicted in Fig. 6(b), the EL spectrum displayed a relatively weak emission at 480 nm and a dominant peak at 620 nm, indicative of red emission. The corresponding color coordinates are shown in Fig. S15(b) in the ESM. These results, when considered alongside the photophysical characterizations, confirm that CD@SiO_2@B_2O_3-2 and CD@SiO_2@B_2O_3-RhB contribute distinct fluorescence and phosphorescence emissions covering green, yellow, and red spectral regions.

To achieve white light emission, the emission ratio of CD@SiO_2@B_2O_3-2 to CD@SiO_2@B_2O_3-RhB was optimized. Coating both materials onto a 365 nm LED chip yields an EL spectrum spanning 460 to 650 nm (Fig. S15(c) in the ESM), effectively covering the green-to-red spectrum. The resulting Commission Internationale de l'Éclairage (CIE) chromaticity coordinates are (0.39, 0.46), with a correlated color temperature (CCT) of 4180 K, falling within the range of warm white light (Fig. S15(d) in the ESM). Further, CD@SiO_2@B_2O_3-2 and CD@SiO_2@B_2O_3-RhB were applied to a commercial 450 nm LED chip. The resulting WLED showed an expanded emission spectrum with an added blue component at 450 nm, as shown in Fig. 6(c). The CIE coordinates were determined to be (0.36, 0.37), with a CCT of 4250 K (Fig. 6(d)), yielding a neutral white light with a slight yellow tint. This warm white emission closely resembles natural daylight during morning or late afternoon, providing a soft and eye-friendly

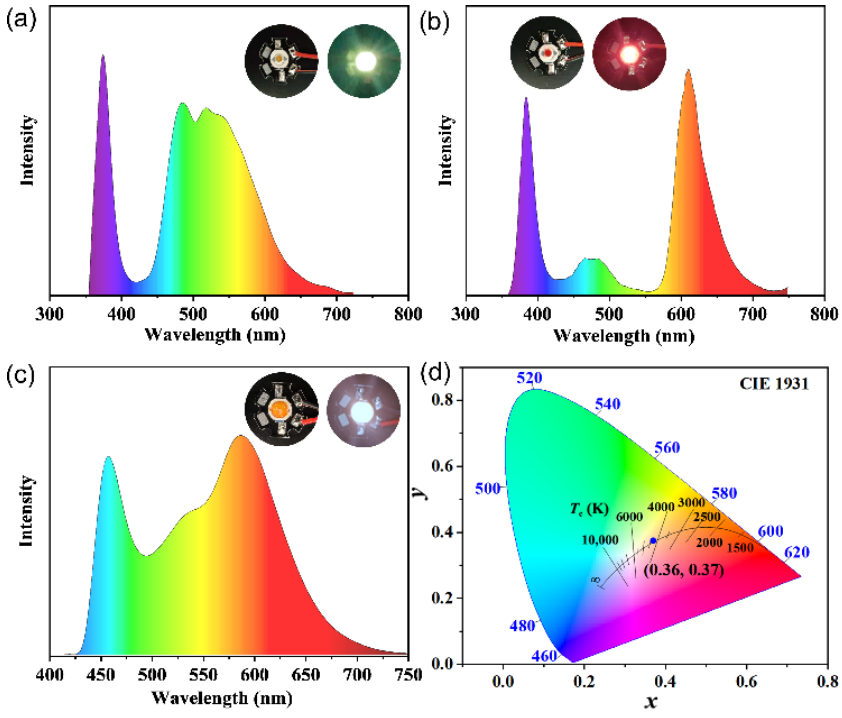

Figure 6 (a) EL spectrum of CD@SiO_2@B_2O_3-2. (b) EL spectrum of CD@SiO_2@B_2O_3-RhB. (c) EL spectrum of the mixture of CD@SiO_2@B_2O_3-2 and CD@SiO_2@B_2O_3-RhB. Insets of ((a)–(c)): photographs of LEDs (Ex: 365, 365, and 450 nm) under daylight and being on state. (d) CIE chromaticity diagram of the color coordinates of the EL emission.

illumination suitable for prolonged usage in work or study environments.

Importantly, this WLED configuration achieves warm white light emission without the incorporation of any commercial phosphors, a distinct advantage over many conventional systems that require such additives [53]. These results underscore the great promise of CD@SiO_2@B_2O_3-based materials in next-generation solid-state lighting and energy-efficient WLED applications.

4 Conclusions

In this study, we significantly enhanced the RTP performance of carbon dots through a multiscale-coupled triple-confinement strategy. By integrating molecular-level covalent linking (C=N bonds), nanoscale silica encapsulation, and a rigid boron oxide matrix, the as-prepared CD@SiO_2@B_2O_3 composites achieve a remarkably prolonged phosphorescence lifetime of up to 1119.8 ms and a high quantum yield of 25.98%, far exceeding those of singly confined CDs. This remarkable enhancement is attributed to the synergistic restriction of molecular motion by the triple-confinement effects, which efficiently suppress non-radiative relaxation and stabilize triplet excitons. The strategy demonstrates excellent versatility and can be readily extended to other carbon sources and confining agents, affording comparable improvements of phosphorescence lifetime. Moreover, by doping trace amounts of RhB and RhG dyes (1 wt.%) based on the phosphorescence resonance energy transfer effect mechanism, tunable multicolor RTP emission is successfully realized. These merits enable promising applications in information encryption, fingerprint recognition, multicolor anti-counterfeiting, and fabrication of warm white light-emitting diodes. These findings not only showcase the excellent application prospects of the as-developed RTP materials but also offer a reliable and universal platform for developing high-performance RTP CDs.

Electronic Supplementary Material: Supplementary material (Figs. S1–S15, Tables S1–S10, experimental details, and six video clips of luminous phenomena that change over time) is available in the online version of this article at https://doi.org/10.26599/NR.2026.94908629.

Data availability

All data needed to support the conclusions in the paper are presented in the manuscript and the Electronic Supplementary Material. Additional data related to this paper may be requested from the corresponding author upon request.

Acknowledgements

We acknowledge the financial support from the National Natural Science Foundation of China (Nos. 22572115 and 22272101), the National Key Research and Development Program of China (No. 2022YFA1205502), and the Xi'an Key Laboratory of CBRN Smart Sensing.

Declaration of competing interest

All the contributing authors report no conflict of interests in this work.

Author contribution statement

K. X. C.: Writing – original draft, visualization, methodology, investigation, data curation, conceptualization. K. Y. X.: Investigation, data curation. H. N. P.: Writing – original draft, visualization, supervision. L. P. D.: Writing – review & editing, writing – original draft, supervision, resources, funding acquisition, conceptualization. Y. F.: Writing – review & editing, supervision.

Use of AI statement

None.

References

[1] Zhang, T.; Ma, X.; Wu, H. W.; Zhu, L. L.; Zhao, Y. L.; Tian, H. Molecular engineering for metal-free amorphous materials with room-temperature phosphorescence. *Angew. Chem., Int. Ed.* **2020**, *59*, 11206–11216.

[2] Zheng, H.; Zhang, Z. Y.; Cai, S. Z.; An, Z. F.; Huang, W. Enhancing purely organic room temperature phosphorescence via supramolecular self-assembly. *Adv. Mater.* **2024**, *36*, 2311922.

[3] Gu, F.; Ji, M. X.; Zhang, L. S.; Zhao, T. J.; Zhang, R. Q.; Lv, X.; Tian, H.; Ma, X. Visualization of photocuring and 4D printing with real-time phosphorescence. *Nat. Commun.* **2025**, *16*, 4173.

[4] Huang, Q. Q.; Gao, H. Q.; Yang, S. M.; Ding, D.; Lin, Z. H.; Ling, Q. D. Ultrastable and colorful afterglow from organic luminophores in amorphous nanocomposites: Advanced anti-counterfeiting and *in vivo* imaging application. *Nano Res.* **2020**, *13*, 1035–1043.

[5] Zhang, X. P.; Liu, J. K.; Chen, B.; He, X. W.; Li, X. Y.; Wei, P. F.; Gao, P. F.; Zhang, G. Q.; Lam, J. W. Y.; Tang, B. Z. Highly efficient and persistent room temperature phosphorescence from cluster exciton enables ultrasensitive off-on VOC sensing. *Matter* **2022**, *5*, 3499–3512.

[6] Zhou, Z. X.; Wang, X.; Lv, A. Q.; Ding, M. J.; Song, Z. C.; Ma, H. L.; An, Z. F.; Huang, W. Achieving efficient X-ray scintillation of purely organic phosphorescent materials by chromophore confinement. *Adv. Mater.* **2024**, *36*, 2407916.

[7] Wang, X. H.; Pan, G. C.; Ren, H. X.; Li, J. S.; Xu, B.; Tian, W. J. Reversible photoswitching between fluorescence and room temperature phosphorescence by manipulating excited state dynamics in molecular aggregates. *Angew. Chem., Int. Ed.* **2022**, *61*, e202114264.

[8] Lee, O. S.; McKay, A. P.; Cordes, D. B.; Warriner, S. L.; Gather, M. C.; Zysman-Colman, E. Simultaneous multi-resonant thermally activated delayed fluorescence and room temperature phosphorescence from biluminescent nitrogen-containing indolocarbazoles. *Adv. Sci.* **2025**, *12*, e03175.

[9] Ma, L. W.; Liu, Y. W.; Jin, X.; Jiang, T.; Zhou, L.; Wang, Q. C.; Tian, H.; Ma, X. Triplet exciplex mediated multi-color ultra-long afterglow materials. *Angew. Chem.* **2025**, *137*, e202500847.

[10] Han, X.; Zheng, H. Q.; Yang, Y.; Cui, Y. J.; Qian, G. D. Tunable room-temperature phosphorescence in hydrogen-bonded organic crystals via H-bonding units. *Adv. Funct. Mater.* **2025**, *35*, 2425934.

[11] Hou, L. H.; Wang, T.; Yu, S.; Xu, X. H.; Yu, X. Multiresponsive color-tunable phosphorescence with matrix-confined clusters. *Aggregate* **2025**, *6*, e70071.

[12] Zhang, Y. W.; Gao, M. X.; Wu, R. M.; Meng, Y. S.; Li, N.; Chen, Z. J.; Fang, M. M.; Yang, J.; Li, Z. Adjustable room-temperature phosphorescence through tunable aggregation of dopants in polymers and its application in hydrazine hydrate detection. *Adv. Funct. Mater.* **2025**, *35*, 2502811.

[13] Jiang, K.; Wang, Y. C.; Lin, C. J.; Zheng, L. C.; Du, J. R.; Zhuang, Y. X.; Xie, R. J.; Li, Z. J.; Lin, H. W. Enabling robust and hour-level organic long persistent luminescence from carbon dots by covalent fixation. *Light Sci. Appl.* **2022**, *11*, 80.

[14] Gan, N.; Shi, H. F.; An, Z. F.; Huang, W. Recent advances in polymer-based metal-free room-temperature phosphorescent materials. *Adv. Funct. Mater.* **2018**, *28*, 1802657.

[15] Qiu, H.; Yan, Y. Q.; Zhou, H.; Gao, Z. H.; Chen, S. W.; Zhu, C. F.; Wang, Z. F. Stimuli-responsive metal-free phosphorescent materials: From design and mechanisms to emerging applications. *Coord. Chem. Rev.* **2025**, *538*, 216734.

[16] Liu, Y. P.; Cheng, D. K.; Wang, B. Z.; Yang, J. X.; Hao, Y. M.; Tan, J.; Li, Q. J.; Qu, S. N. Carbon dots-inked paper with single/two-photon excited dual-mode thermochromic afterglow for advanced dynamic information encryption. *Adv. Mater.* **2024**, *36*, 2403775.

[17] Hu, Y. L.; Seivert, O.; Tang, Y.; Karahan, H. E.; Bianco, A. Carbon dot synthesis and purification: Trends, challenges and recommendations. *Angew. Chem., Int. Ed.* **2024**, *63*, e202412341.

[18] Ding, L.; Jin, X. L.; Gao, Y. C.; Kang, S. W.; Bai, H. Y.; Ma, X. H.; Ai, T. T.; Zhou, H. W.; Chen, W. X. Novel strategy of multidimensional information encryption via multi-color carbon dots aggregation-induced emission. *Nano Res.* **2024**, *17*, 5680–5687.

[19] Yu, Y.; Zeng, Q. S.; Tao, S. Y.; Xia, C. L.; Liu, C. M.; Liu, P. Y.; Yang, B. Carbon dots based photoinduced reactions: Advances and perspective. *Adv. Sci.* **2023**, *10*, 2207621.

[20] Wen, J. L.; Zeng, Z. F.; Wang, B. L.; Hong, J. Y.; Chen, Y. Y.; Zhang, J. Y.; Li, J. Y.; Jiang, J. X. Modulating hydrothermal condition to achieve carbon dots-zeolite composites with multicolor afterglow. *Nano Res.* **2023**, *16*, 7761–7769.

[21] Zhang, Y. Q.; Liu, Y.; Ren, X. Y.; Kang, Y. H.; Ding, S. R.; Lu, S. Y. Adjusting TADF and phosphorescence for tailored dynamic time-dependent afterglow colored carbon dots spanning full visible region. *Angew. Chem., Int. Ed.* **2025**, *64*, e202421421.

[22] Zhao, Q. L.; Fan, C. Y.; Bu, H.; Gao, J.; Li, L. L.; Yu, X. F.; Yang, X. J.; Lu, Z. M.; Zhang, X. H. Electrochemical synthesis of multicolor carbon dots with room temperature phosphorescence to thermally activated delayed fluorescence via surface state modulation. *Chem. Eng. J.* **2024**, *500*, 156704.

[23] Hu, H. J.; Li, J. R.; Gong, X. Hour-level persistent multicolor phosphorescence enabled by carbon dot-based nanocomposites through a multi-confinement-based approach. *Small* **2024**, *20*, 2308457.

[24] Ding, Y. F.; Wang, X. L.; Tang, M.; Qiu, H. B. Tailored fabrication of carbon dot composites with full-color ultralong room-temperature phosphorescence for multidimensional encryption. *Adv. Sci.* **2022**, *9*, 2103833.

[25] Li, J.; Zhou, H.; Qiu, H.; Yan, Y. Q.; Wang, X.; Gao, Z. H.; Wang, Z. F. Phosphorescent carbon dots: Intermolecular interactions, properties, and applications. *Coord. Chem. Rev.* **2024**, *503*, 215642.

[26] Sun, W. X.; Zhang, Y. Q.; Yin, G. C.; Lu, S. Y. Afterglow of dual-confined carbon dots ranging from blue to near-infrared. *Adv. Funct. Mater.* **2024**, *34*, 2402346.

[27] Zhu, S. J.; Song, Y. B.; Zhao, X. H.; Shao, J. R.; Zhang, J. H.; Yang, B. The photoluminescence mechanism in carbon dots (graphene quantum dots, carbon nanodots, and polymer dots): Current state and future perspective. *Nano Res.* **2015**, *8*, 355–381.

[28] Zhou, S. J.; Wang, F. X.; Feng, N.; Xu, A. X.; Sun, X. F.; Zhou, J. H.; Li, H. G. Room temperature phosphorescence carbon dots: Preparations, regulations, and applications. *Small* **2023**, *19*, 2301240.

[29] Liu, Z. P.; Ding, X. B.; Cai, L.; Jia, Y. H.; Ran, X.; Guo, Z. Z.; Mo, D.; Pan, Y. T.; Guo, L. J. Cascade energy transfer endows phosphorescent carbon dots-based films with tunable and broadband afterglow for fingerprint recognition and anticounterfeiting. *Chem. Eng. J.* **2025**, *506*, 160311.

[30] Chen, J. Y.; Tan, J. Q.; Liang, P.; Wu, C. J.; Hou, Z. L.; Shen, K. Y.; Lei, B. F.; Hu, C. F.; Zhang, X. J.; Zhuang, J. L. et al. Dynamic room temperature phosphorescence of silane-functionalized carbon dots confining within silica for anti-counterfeiting applications. *Small* **2024**, *20*, 2306323.

[31] Li, J. R.; Zhao, X. J.; Gong, X. Rational design of dual-mode emitting carbon dots to exploit the synergistic effect of matrices for high-efficiency WLEDs and anti-counterfeiting. *Adv. Opt. Mater.* **2024**, *12*, 2302297.

[32] Shi, H. X.; Wu, Y.; Xu, J. H.; Zhou, C. F.; Xu, H.; Ye, W. P.; Yin, Y. F.; Wang, Z. Y.; Su, R. F.; An, Z. F. et al. Enhancing blue phosphorescence in matrix-free carbon dots through covalent crosslinking. *Chem. Eng. J.* **2023**, *476*, 146524.

[33] Fu, M.; Lin, L. Q.; Wang, X.; Yang, X. M. Hydrogen bonds and space restriction promoting long-lived room-temperature phosphorescence and its application for white light-emitting diodes. *J. Colloid Interface Sci.* **2023**, *639*, 78–86.
[34] Lv, W. H.; Cao, Q.; Song, S. Y.; Liang, Y. C.; Zhou, R.; Liu, K. K.; Shan, C. X. Enhanced phosphorescence of carbon nanodots via double confinement for 3D artworks with long emission lifetimes. *Small* **2023**, *19*, 2302504.
[35] Luo, Y. M.; Jiang, Q.; Liu, J. K.; Huang, F. Y.; Liao, X. L.; Zhuang, J. L.; Hu, C. F.; Zheng, M. T.; Lei, B. F.; Liu, Y. L. et al. Multiple confinement-limited activation and defect effect co-triggered the ultra-long lifetime of carbon dots. *Chem. Eng. J.* **2024**, *500*, 156781.
[36] Zhang, Y. Q.; Li, M. Y.; Lu, S. Y. Rational design of covalent bond engineered encapsulation structure toward efficient, long-lived multicolored phosphorescent carbon dots. *Small* **2023**, *19*, 2206080.
[37] Zhang, S. W.; Shen, C. L.; Li, J. R.; Liao, J. F.; Miao, P.; Zhao, X. J.; Gong, X. Ultra-wide time-dependent phosphorescence color of carbon dots via a synergistic strategy of dual confinement structures constructing multiple luminescent centers. *Chem. Sci.* **2025**, *16*, 14098–14108.
[38] Cui, K. X.; Chen, Y.; Xie, K. Y.; Peng, H. N.; Ding, L. P.; Fang, Y. Nanoconfined synthesis of $CsPbBr_3$ quantum dots: Enhanced stability, tunable luminescence, and sensitive sensing application. *ACS Appl. Mater. Interfaces* **2025**, *17*, 20075–20086.
[39] Mei, J.; Bao, J.; Cheng, X.; Ren, D. D.; Xu, G. H.; Wei, F. D.; Sun, Y.; Hu, Q.; Cen, Y. Novel dual-emissive fluorescent silicon nanoparticles for detection of enzyme activity in supplements associated with lactose intolerance. *Sens. Actuators B: Chem.* **2021**, *329*, 129164.
[40] Cui, K. X.; Tang, Q. X.; Zhao, T. Y.; Qiao, M.; Peng, H. N.; Ding, L. P.; Fang, Y. Bifunctional mesoporous silica nanoparticles with europium(Ⅲ) and pyrene for visual detection and discriminative identification of six fluoroquinolone antibiotics. *Sens. Actuators B: Chem.* **2025**, *427*, 137162.
[41] Li, Q. J.; Cheng, D. K.; Gu, H. L.; Yang, D. Q.; Li, Y. C.; Meng, S.; Zhao, Y. Y.; Tang, Z. K.; Zhang, Y. B.; Tan, J. et al. Aggregation-induced color fine-tunable carbon dot phosphorescence covering from green to near-infrared for advanced information encryption. *Chem. Eng. J.* **2023**, *462*, 142339.
[42] Li, Y. C.; Li, Q. J.; Meng, S.; Qin, Y. K.; Cheng, D. K.; Gu, H. L.; Wang, Z. F.; Ye, Y. X.; Tan, J. Ultrabroad-band, white light emission from carbon dot-based materials with hybrid fluorescence/phosphorescence for single component white light-emitting diodes. *Chin. Chem. Lett.* **2023**, *34*, 107794.
[43] Li, Q. J.; Zhao, Z. X.; Meng, S.; Li, Y. C.; Zhao, Y. Y.; Zhang, B. H.; Tang, Z. K.; Tan, J.; Qu, S. N, Ultra-strong phosphorescence with 48% quantum yield from grinding treated thermal annealed carbon dots and boric acid composite. *SmartMat* **2022**, *3*, 260–268.
[44] Li, R.; Zhang, L. P.; Fan, J.; Wang, B. J.; Xu, H.; Mao, Z. P. Synergistic confinement and heavy atom effects in carbon dots for enhanced phosphorescence: Matrix-free and matrix conditions. *Chem. Eng. J.* **2025**, *526*, 171205.
[45] Cui, K. X.; Qiao, M.; Xu, W.; Yan, Z.; Peng, H. N.; Ding, L. P.; Fang, Y. Silica nanoparticle-based FRET system for hydrogen sulfide detection in biological and food samples. *ACS Appl. Nano Mater.* **2024**, *7*, 11739–11748.
[46] Feng, Q.; Xie, Z. G.; Zheng, M. Colour-tunable ultralong-lifetime room temperature phosphorescence with external heavy-atom effect in boron-doped carbon dots. *Chem. Eng. J.* **2021**, *420*, 127647.
[47] Ran, X.; Pan, Y. T.; Qiao, L. L.; Cai, L.; Jia, Y. H.; Liu, Z. P.; Guo, L. J. Broadband and dynamic afterglow photoluminescent carbon dots for time-resolved optical information coding and encryption. *Carbon* **2025**, *234*, 119980.
[48] Lou, Q.; Chen, N.; Zhu, J. Y.; Liu, K. K.; Li, C.; Zhu, Y. S.; Xu, W.; Chen, X.; Song, Z. J.; Liang, C. H. et al. Thermally enhanced and long lifetime red TADF carbon dots via multi-confinement and phosphorescence assisted energy transfer. *Adv. Mater.* **2023**, *35*, 2211858.
[49] Yin, G. Q.; Lu, W.; Huang, J. X.; Li, R.; Liu, D. P.; Li, L. Q.; Zhou, R. H.; Huo, G. F.; Chen, T. Ultralong excimer phosphorescence by the self-assembly and confinement of terpyridine derivatives in polymeric matrices. *Aggregate* **2023**, *4*, e344.
[50] Liang, Y. C.; Cao, Q.; Liu, K. K.; Peng, X. Y.; Sui, L. Z.; Wang, S. P.; Song, S. Y.; Wu, X. Y.; Zhao, W. B.; Deng, Y. et al. Phosphorescent carbon-nanodots-assisted Förster resonant energy transfer for achieving red afterglow in an aqueous solution. *ACS Nano* **2021**, *15*, 16242–16254.
[51] Xu, Z. X.; Chen, W. B.; Chen, K. Y.; Lin, S. W.; Wu, Z. Y.; Deng, G. Q.; Chen, J. C.; Tayyab, M.; Xiong, Y.; Li, M. D. et al. Stimulus-responsive emission via dynamic triplet energy transfer in organic room-temperature phosphorescence glass. *Adv. Mater.* **2025**, *37*, 2418778.
[52] Peng, X. L.; Zou, P.; Zeng, J. J.; Wu, X.; Xie, D.; Fu, Y.; Yang, D. Z.; Ma, D. G.; Tang, B. Z.; Zhao, Z. J. Purely organic room-temperature phosphorescence molecule for high-performance non-doped organic light-emitting diodes. *Angew. Chem., Int. Ed.* **2024**, *63*, e202405418.
[53] Zhao, L. L.; Zhang, H.; Wang, L.; Liu, W. P.; Wang, X. S.; Li, B.; Lin, Q. L.; Fan, F. J.; Shen, H. B. Bright and stable green quantum dot light-emitting diodes via increasing electron concentration. *Nano Res.* **2025**, *18*, 94907978.